Journal of Sound and Vibration (2001) **244**(1), 79–106
doi:10.1006/jsvi.2000.3459, available online at http://www.idealibrary.com on IDEAL®

CHARACTERIZATION OF RASPING NOISE IN AUTOMOTIVE ENGINE EXHAUST DUCTS

M. Ayadi, S. Frikha and P.-Y. Hennion

Laboratoire de Mécanique Physique UPRESA CNRS 7068, *Université Pierre et Marie Curie*, 2 *Place de la gare de Ceinture*, 78210 *Saint Cyr l'Ecole*, *France*

and

R. Willats

Arvin–Exhaust Advanced Technologies, *England*

(*Received* 5 *June* 2000, *and in final form* 18 *October* 2000)

This paper presents an experimental study of a non-linear acoustic phenomenon resulting in the generation of a large high component in the automotive engine exhaust system. This phenomenon may occur when an engine is submitted to an abrupt acceleration. The perceived noise, known as "rasping noise" has a metallic and strident tone. The results of frequency and wavelet analysis of the tailpipe noise are presented. Both of them show that a high-frequency component is instantaneously generated at a critical engine speed. An efficient criterion based on multiresolution wavelet analysis is proposed in order to detect the rasping occurrence and quantify the rate of high-frequency component in the tailpipe noise. The obtained results are well correlated with subjective analysis. The analysis of the internal pressure along the exhaust pipe shows that the rasping noise is generated in the intermediate tube and that the acoustic pressure measured at the exit of the manifold does not contain any high-frequency component. The authors favour the hypothesis of non-linear coupling between resonance modes which explains the sensitivity of the rasping noise generation to the slope of the acceleration.

1. INTRODUCTION

The non-linear phenomena caused by finite amplitude waves travelling in pipes and ducts are often neglected in predictive acoustic analyses because they significantly increase the computation cost. Nevertheless, in several cases, they fundamentally modify the response of the system especially when they are associated with resonance modes. These effects concern not only the amplitude of the piping system response but also its frequency spectrum. Namely, the tone of the sound delivered at the tailpipe may be strongly affected by a non-linear behaviour.

In this subject, the work of Chester [1] remains the most famous. He developed an analytical solution of the non-linear resonance of a viscous closed tube and showed that wave discontinuities may be generated. He also showed that these discontinuities are significantly softened by viscous effects. The balance between the source strength and the viscous effects then determines if a non-linear model should be considered.

Such phenomena are of great interest when dealing with a wind music instrument [2]. Typically, the high pitched component characterizing the tone of a brass instrument is shown to be caused by the non-linear propagation of sound waves [3].

0022-460X/01/260079 + 28 $35.00/0

Another field where the non-linear effects may strongly modify the acoustic response of a piping system is the automotive exhaust path. In fact, the improvement of engine efficiencies is of an increasing interest to car manufacturers. One parameter that has an important effect on the engine performance is the static pressure at the exit of the engine exhaust valve. It is the well-known engine "backpressure". In the new generation of powerful engines, there is a tendency to lower that backpressure to enhance engine performance. This induces an increase of the acoustic pressure level at the exit of the manifold (180 dB, referenced to 20 μPa) due to the increased pressure difference downstream and upstream of the exhaust valve especially during rapid acceleration. The exhaust system manufacturers have the difficult task of reducing that sound level to 100 dB at the tailpipe.

Moreover, from a subjective point of view, the tone of a vehicle exhaust noise becomes a significant factor in the customer's judgement. Thus, as the exhaust noise becomes quieter in level, the psycho-acoustic criteria become increasingly significant. That means that, in addition to reduction of its total level, the noise spectral contents in terms of low and high frequencies must be analyzed and optimized.

Besides these requirements, the exhaust system designers need to work within the constraint that the total volume allocated to the exhaust line is increasingly small, especially in the small car, B car or town car segment. In this case the exhaust systems classically equipped with three boxes (catalytic converter, sub-muffler and main muffler) are replaced by exhaust lines equipped with only two boxes (catalytic converter and main muffler). This implies the use of a long intermediate pipe and favours the formation of standing waves at lower frequencies. In normal conditions, these kinds of exhaust systems work perfectly and conform to design specifications. However, some experiments performed in exacting conditions subjectively show that these exhaust systems may generate an undesirable sound that is characterized by its intermittence and by a metallic aspect particularly irritating to the human ear. This undesirable sound known as "rasping noise" contributes to the global noise emitted by the exhaust system and therefore may have to be taken into account in the pass-by noise computation. When rasping noise occurs it gives the impression of mechanical rattle, and so gives an impression of poor quality.

A primary investigation of this phenomenon has shown that the rasping noise occurs when a powerful engine is started and quickly accelerated under cold conditions. It is greatly reduced when the engine and the exhaust system are warmed up. Rasping noise does not normally occur with constant engine speed or slow run up.

In previous work on this subject, the rasping noise is assumed to be caused by shock waves generated inside the exhaust pipe. Nirei *et al.* [4] postulated that a third of the rasping noise is emitted to the atmosphere as a shell radiation noise whereas the remaining part is emitted through the exhaust tailpipe orifice. However Okada *et al.* [5, 6] postulated that the total rasping noise is emitted through the exhaust outlet into the still atmosphere despite the fact that the associated metallic tone is perceived as radiation noise caused by vibration of the outer shell of the muffler. Okada *et al.* also showed that the finite amplitude compressive waves generated downstream of the exhaust valve and amplified by resonance are steepened as they travel along the pipe. These non-linear effects hence defined give rise to shock waves after passing a distance called the transition distance which was analytically defined. In another case, Takayama *et al.* [7] visualized the flow at the vicinity of a sudden area expansion within a simple exhaust pipe. They demonstrated by solving the unsteady two-dimensional Euler equations that a planar shock wave occurs at the smallest section of the expansion area. It is diffracted at the corner of the area expansion and turns into cylindrical shock, which attenuates with propagation. Jonas *et al.* [8] studied the rasping noise as a part of

the exhaust noise radiated by the outer shell of mufflers. They tested the rasping noise generation on various muffler configurations.

This paper presents the results of an experimental study concerned with the characterization of the rasping noise. The focus here is on developing an objective criterion for the detection and the quantitative assessment of the metallic component. The acoustic signatures of a large set of exhaust systems were collected at various running conditions. Simultaneously, the tailpipe sounds were perceived and subjectively estimated as to whether or not they include a raspy component. The measurements were performed during more or less abrupt engine run up which led to non-stationary signals. Three types of processing are tested here. The first and the second processing are based on Fourier spectral analysis. The first processing consists of a classical short-time Fourier transform (STFT). The second one is a tracking analysis that takes into account the periodicity of the collected signal and allows synchronization with the engine crank-shaft rotation.

The third processing consists of a decomposition of the signal by using a wavelet basis. As this treatment is less classical and less standardized, a short review of the basic theory is made. Results of both continuous and discrete wavelet analysis are presented. The last one is then used to build a detection criterion that also allows the quantification of the rasping rate within the whole tailpipe noise.

In the last section, the acoustic pressure captured within the exhaust system is examined and an attempt is made to propose a physical interpretation of rasping noise occurrence. The hypothesis of non-linear interaction between resonance modes is favoured.

2. EXPERIMENTAL SET-UP

The experiments presented in this paper were carried out on an engine bench (see Figure 1) composed of a gasoline engine, an electric brake providing a controlled resistive load, and a real exhaust system. The gasoline engine has four cylinders, 2 litres, 16 valves, providing a maximum power of 102 kW at 6000 r.p.m., and maximum torque of 182 Nm at 4500 r.p.m. The burned gas escaped to the atmosphere through a real exhaust line. The wall of the test room constitutes an acoustic baffle providing a separation between the exhaust tailpipe noise and the vibrating engine noise. Otherwise, this exhaust system was connected to the engine manifold by a flexible pipe and mounted on two rigid supports in order to isolate the exhaust line from the engine vibrations.

The backpressure or the static pressure at the engine manifold is a parameter that affects the efficiency of the engine. Its value is affected by the geometrical configuration of the exhaust system. As the engine is considered as an acoustic source, the focus was on having the same acoustic source features in all experiments. For that reason the measurement and control of the backpressure was an important task. It was measured by using a gauge pressure sensor at the exit of the manifold. A cavity was inserted between the pressure pick-up and the sensor to filter the dynamic component and to estimate the mean pressure with respect to the engine rotational speed. The pressure gauge signal was acquired by using a National Instrument acquisition board. Then a Butterworth IIR low-pass filter with a cut-off frequency of 50 Hz, based on a 1 kHz sampling frequency, was applied to eliminate the higher frequency components.

The acoustic pressure was collected by using five—PCB type 106B—piezoelectric transducers, flush-mounted in the wall of the exhaust line as shown in Figure 1. These sensors have a dynamical range of 57 kPa (189 dB, referenced to 20 μPa) and a cut-off frequency of 60 kHz allowing a high-frequency analysis of measured pressures. They were water-cooled in order to maintain their temperature to less than 120°C. The first sensor was

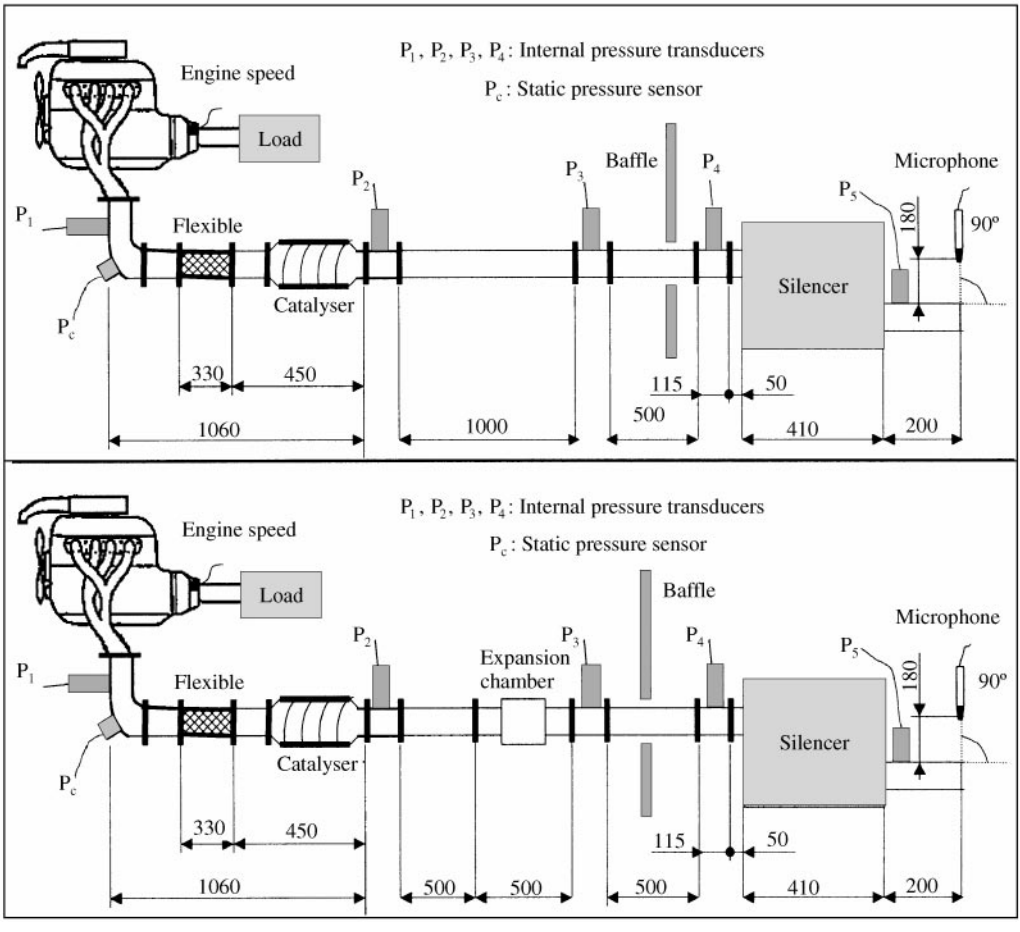

Figure 1. Experimental set-up. Upper, critical exhaust line producing rasping noise; lower, classic exhaust line producing a normal tone.

located at the exit of the manifold in order to analyze the engine pressure source. Three sensors were positioned along the intermediate pipe in order to track the rasping noise generation when it occurs. The last sensor was located at the outlet of the rear muffler. In addition, a 1/4 B&K microphone (type 2671, cut-off frequency, flat within ± 1 dB: 20 kHz, upper dynamic range: 172 dB, sensitivity: 1·27 mV/Pa) was used to measure the tailpipe noise emitted in the atmosphere 18 cm away from the exhaust outlet.

The signals from the piezoelectric sensors and the tailpipe microphone were acquired and post-processed by using an 8-channel HP35650B signal analyzer. They were sampled with a frequency of 32·768 kHz. In order to get an RPM reference channel, a tachometric signal provided by a magnetic sensor mounted on the engine crank-shaft was acquired. The post-processing of the acoustic pressure signals consisted both of frequency and order analysis. The time sampling frequency allowed a frequency analysis up to 12·8 kHz and an order analysis up to the 100th harmonic.

A set of exhaust systems composed of a catalytic converter and a rear muffler with or without expansion chamber were used under various conditions (acceleration slope, temperature, load etc.). The rasping noise was heard for a few critical exhaust lines and severe run-up conditions. The focus was on the correlation between the subjective

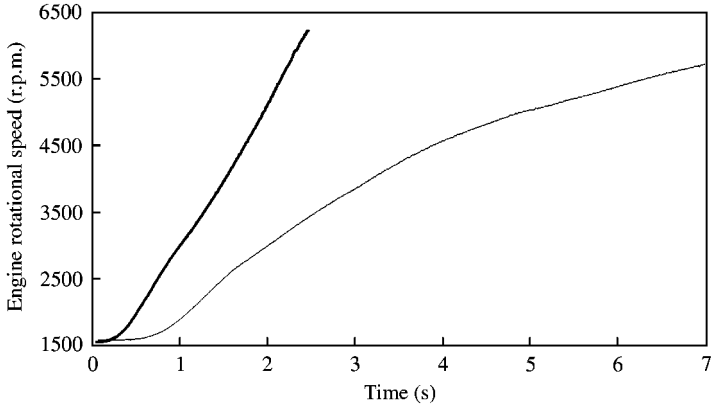

Figure 2. Engine r.p.m. profile. Thick lines, fast run-up, rasping case; thin lines, slow run-up, no-rasping case.

appreciation and the objective analysis of that abnormal exhaust noise. Two configurations are considered in this paper as an example illustrating this correlation. In both cases, the measurements were performed in cold conditions. In the first one, referred to as "rasping case", an abrupt run-up as shown in Figure 2 was chosen. The exhaust pipe comprised a catalytic converter and only one rear muffler. Subjectively, a metallic tone was clearly distinguished for engine speeds roughly higher than 3000 r.p.m. On the other hand, in the second configuration, referred to as "no-rasping case", a slow run-up producing a normal tone was performed. In addition, a sub-muffler was inserted between the catalytic converter and the rear muffler.

3. FREQUENCY AND ORDER ANALYSIS

3.1. FREQUENCY ANALYSIS

The transducer signals from the exhaust lines were acquired during engine run-up, as well as run-down. The fast Fourier transform which is well adapted to stationary signals, does not provide tangible information to interpret correctly these transient phenomena. During the engine run-up and run-down, respectively, the frequencies vary in a continuous way as the engine rotational speed rises or falls. The short-time Fourier transformation (STFT) should be in that case an efficient tool in interpreting these signals. It provides a time–frequency representation that allows the visualization of the time evolution of frequency components during acceleration and deceleration. However, the length and the shape of the window critically determines the time resolution afforded by the STFT.

Figure 3 shows the time–frequency graph of the tailpipe noise in both rasping and no-rasping cases. The upper graph exhibits a large frequency content that reaches 10 kHz with a sound pressure level (SPL) higher than 80 dB and 6 kHz with an SPL higher than 90 dB. This is clearly observed for engine rotational speeds exceeding 3300 r.p.m. One can distinguish a set of constant frequency lines which look like resonance frequencies of the exhaust pipe. On the other hand, the lower graph corresponding to the no-rasping case shows that the frequency content is limited to the low frequency components. Figure 4 provides a zoom on frequencies lower than 1·5 kHz and presents the same result using a full linear scale in order to exhibit better how the signal power is spread over the low frequency range. Both graphs highlight a set of white oblique lines corresponding to the multiple of the

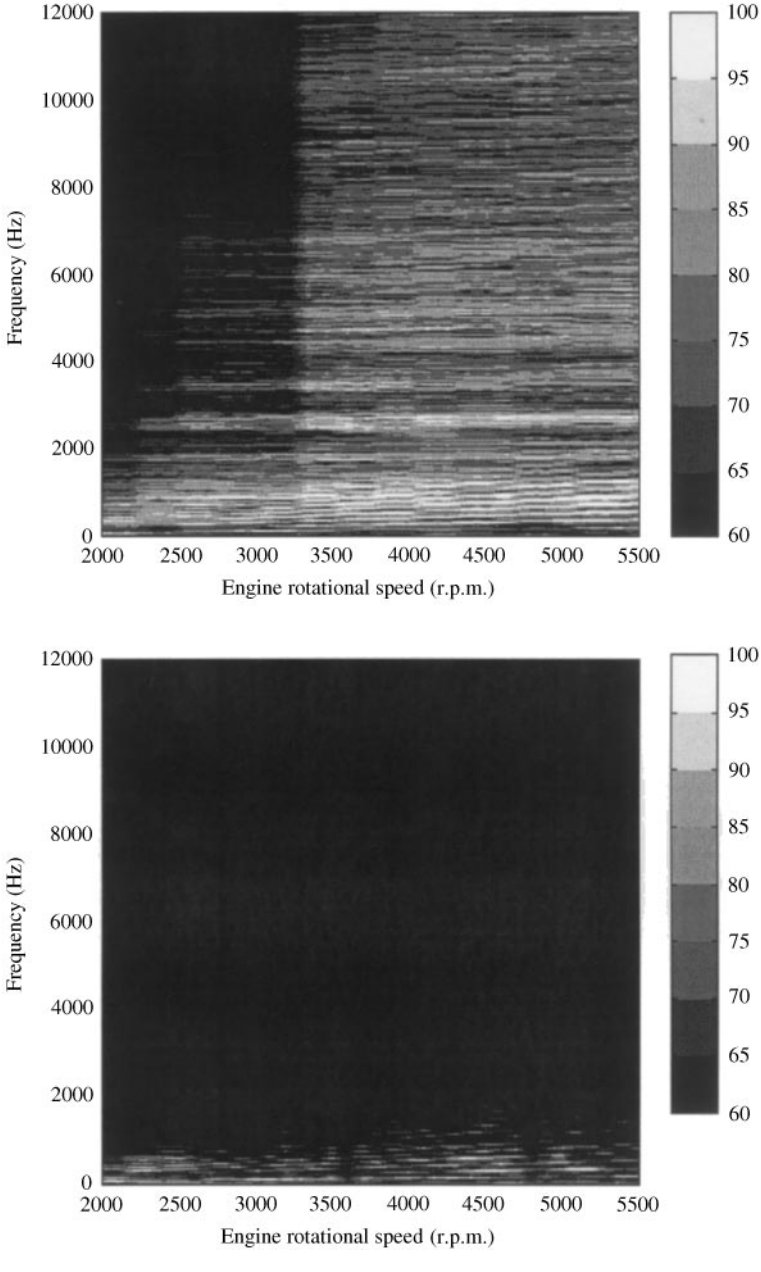

Figure 3. Frequency–r.p.m. plot of the sound pressure level of the tailpipe noise (dB scale). Upper, rasping case; lower, no-rasping case.

crank-shaft rotational frequency. In the no-rasping case, only a few even harmonics are dominating the signal. In fact, it is well known that, in the case of a four cylinder engine equipped with a symmetric manifold, the noise generated into the exhaust system is composed only of even harmonics, especially the second, the fourth and the sixth ones [9]. Otherwise, in the rasping-case, many more harmonics have high levels. Within the engine speed range where rasping noise has been perceived, the high order harmonics are stronger than the second one, usually dominating classic exhaust noise.

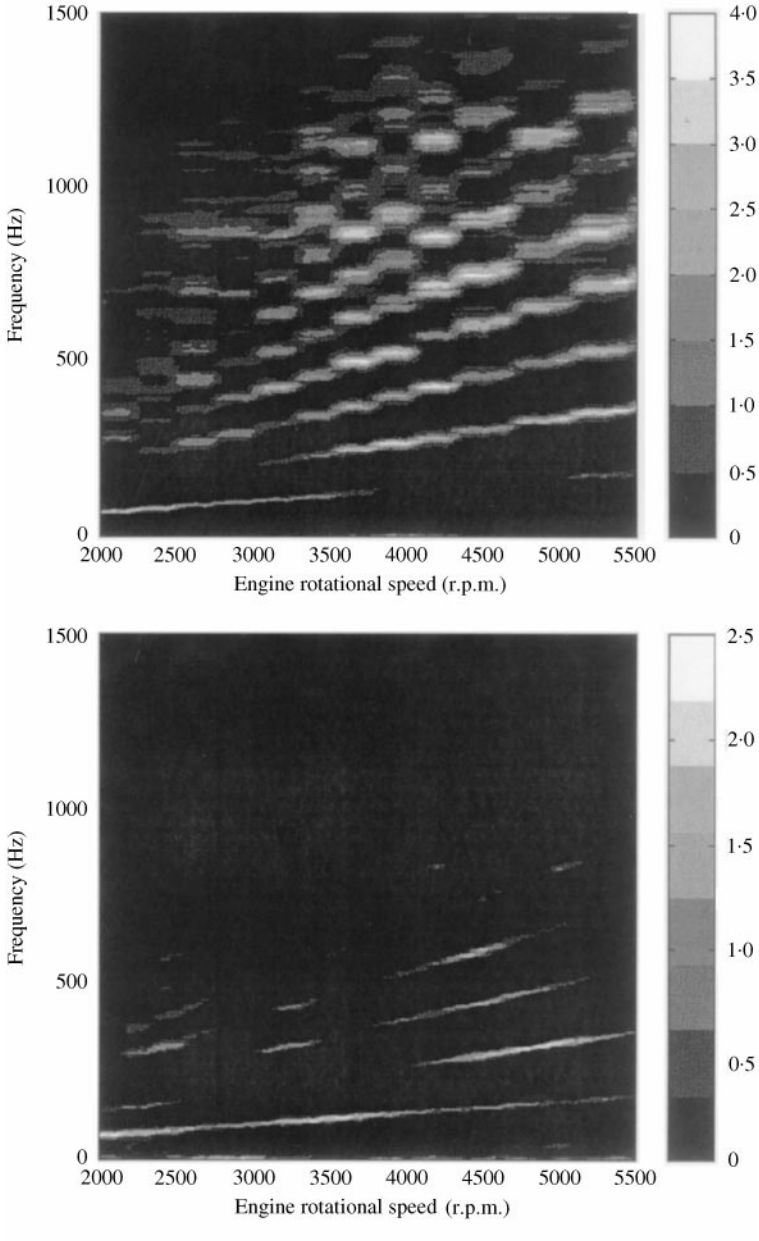

Figure 4. Zoom on low frequencies (0–1500 Hz) of the linear magnitude of the tailpipe noise. Upper, rasping case; lower, no-rasping case. A full z-scale is used in both graphs.

3.2. ORDER ANALYSIS

The main disadvantage of STFT is that it uses a constant time–frequency resolution, and it cannot effectively isolate long time events which need a larger time window. One way to overcome this problem is to calculate the length of such a window according to the frequency to be detected. As the signals processed here may be assumed to be periodic with an instantaneous fundamental frequency changing over an acceleration, the time window

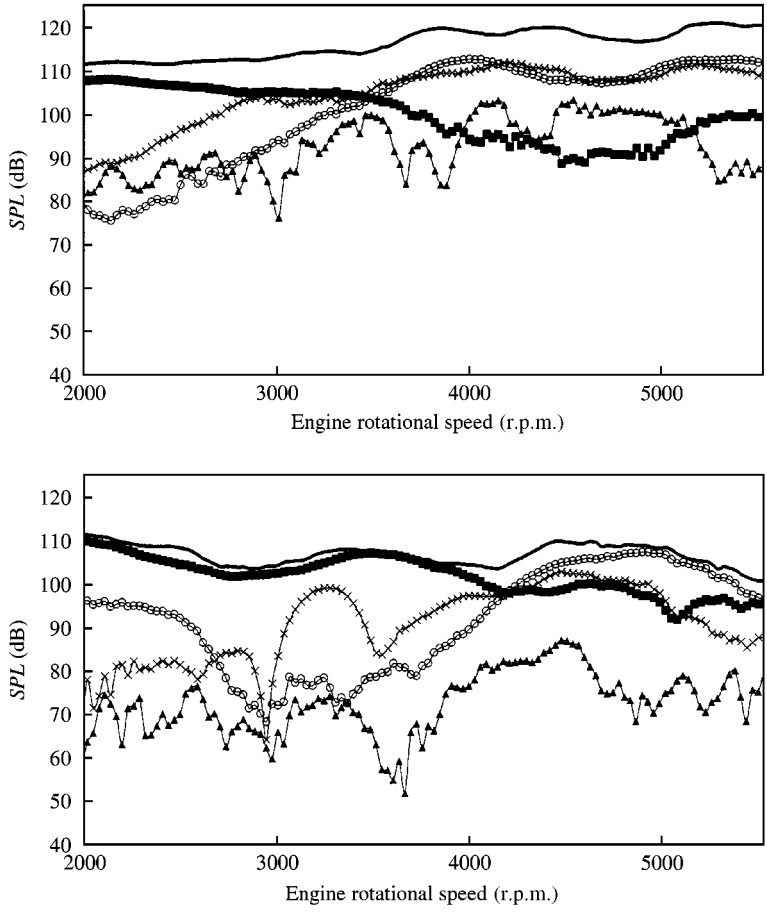

Figure 5. Order tracking of tailpipe noise. Thick solid line; overall noise; square, 2nd harmonics; circle, 4th harmonics; cross, 6th harmonics; triangle, 16th harmonics. Upper, rasping case; lower, no-rasping case.

and the sampling frequency are computed for each engine speed so as to extract the multiples of the fundamental frequency. It results in a tracking procedure and provides an order analysis that is proved to be a more efficient tool in the comprehension of the signal frequency contents. Figure 5 shows the peak to peak level of a set of selected harmonics (H2, H4, H6 and H16) over the engine rotational speed compared to the overall tailpipe microphone signal. In the no-rasping case presented in the lower graph, it is evident that the curve of harmonic H2 almost follows that of the overall noise. Only the fourth harmonic increases for higher engine speeds; the higher ones remain at least 10 dB below. This proves that the total signal energy is concentrated in harmonics H2 and H4. In that case the car exhaust noise is perceived by the human ear as a low-pitched tone. On the other hand, the upper graph obtained in the rasping case highlights a significant gap between the overall noise and both second and fourth harmonics. The signal power is spread over a more broad-frequency band. The curve of H16 is presented as an illustration. It remains 30 dB below the overall noise in the no-rasping case while in the rasping case it significantly grows over the engine rotational speed bandwidth where metallic tone was subjectively noticed.

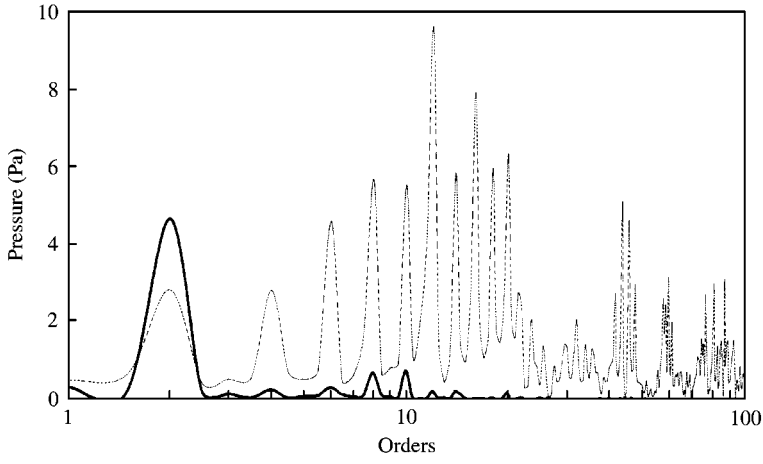

Figure 6. Order contents of the tailpipe noise for a given engine speed of 3500 r.p.m. Dashed curve, rasping case; solid curve, no-rasping case.

Figure 6 shows an example of the order contents at a given engine speed (3500 r.p.m.) in both rasping and no-rasping cases and confirms the comments about Figure 5. It is observed that, while the order contents of the normal noise is dominated by the second harmonic and almost vanishes beyond the 10th, high levels are observed for higher order in the rasping case. Figure 7 shows the order contents as a 2D graph for the whole run-up. The rasping noise is clearly characterized by higher order components occurring from an engine speed of merely 3300 r.p.m. These components are heard by the human ear as a high-pitched tone. Figure 7 also shows hyperbolic white curves that should represent resonance frequencies. Indeed, each of these curves corresponds to a constant frequency which is proportional to the product of the respective projections on the RPM and the order axis.

Regarding the results presented above, the time–frequency plot provides a good estimate of the frequency range characterizing the rasping noise. Otherwise, the r.p.m.-order plot gives a more tidy representation highlighting generated higher harmonics. Indeed, the frequency resolution decreases with respect to the engine rotational speed while the order resolution remains constant.

4. WAVELET ANALYSIS

It was shown in section 3.2, the order tracking analysis allows frequency resolutions that depend on the engine rotational speed. The first harmonics are well analyzed because the corresponding frequencies remain almost constant over each analyzed time window. On the other hand, the frequencies of higher harmonics are significantly changed over the time window:

$$\Delta t = 2\frac{60}{\Omega}, \qquad \Delta\Omega = 2\frac{60\,\mathrm{d}\Omega}{\Omega\,\mathrm{d}t}, \qquad \Delta f(H_k) = \frac{2k\,\mathrm{d}\Omega}{\Omega\,\mathrm{d}t}.$$

Here Δt is the time window width, H_k denotes the kth harmonic, Ω is the engine rotational speed and, with the four-strike-four-cylinder engine considered here, the harmonic resolution is equal to a half the harmonic interval. With reference to Figure 2, as an

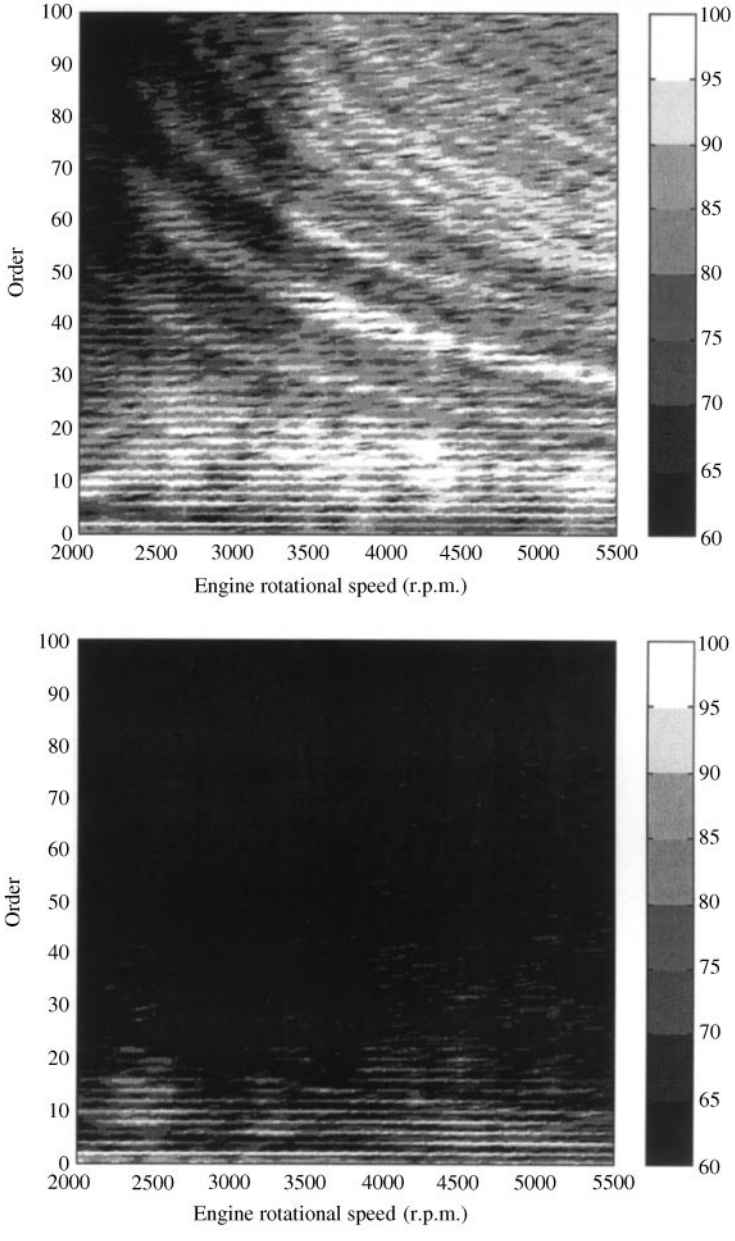

Figure 7. Order analysis of tailpipe noise. Upper, rasping case; lower, no-rasping case.

example, at an engine speed equal to 3000 r.p.m., the time window width is 0·04 s. During this time interval, the engine speed grows over 80 r.p.m. (rapid run-up case) which leads to to a frequency shift $\Delta f(H_k)$ of 66 Hz for the 50th harmonic. So, because the collected signal is non-stationary, the order tracking processing is valid only on a limited frequency span. The Wavelet Transform (WT) overcomes this limitation and enlarges the frequency span by allowing a multiscale analysis. Figure 8 summarizes the corresponding principle. The WT has a fine-frequency resolution for low-frequency components because they are observed

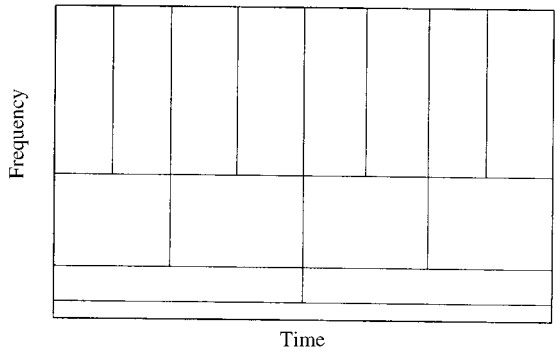

Figure 8. Time–frequency resolution with wavelet analysis.

over a long period. However, higher frequency components are analyzed over shorter periods. This induces a poor-frequency resolution but the time resolution is found to be improved.

4.1. CONTINUOUS WAVELET TRANSFORM (CWT)

The wavelet transform of a signal is an expansion of the signal into a special family of functions referred to as *wavelets* [10]. This family is generated from a single prototype called the mother wavelet by dilation of time and translation along the time axis. The principal feature of wavelet analysis is the ability to explore abrupt changes in non-stationary phenomena. The aim is to understand the correlation between discontinuities, high frequencies and metallic tone in the studied abnormal exhaust noise.

A complex valued function $\psi(t)$ is said to be a wavelet if and only if its Fourier transform $\hat{\psi}(\omega)$ satisfies (a list of principal nomenclature is given in Appendix A)

$$\int_0^{\infty} \frac{|\hat{\psi}(\omega)|^2}{|\omega|}\,\mathrm{d}\omega = C_{\psi} < +\infty. \tag{1}$$

This condition implies that

$$\int_{-\infty}^{+\infty} \psi(u)\,\mathrm{d}u = 0. \tag{2}$$

The mother wavelet $\psi(t)$ may be dilated or contracted by a scale parameter 'a' that is inversely proportional to the frequency. The wavelet is also translated by a time parameter called 'b' which determines the time location of the wavelet. A family of wavelets,

$$\psi_{ab}(t) = a^{-1/2}\psi\left(\frac{t-b}{a}\right), \tag{3}$$

is then generated. The CWT of a function $F(t) \in L_2(\Re)$, $L_2(\Re)$ being the Hilbert space, is defined as

$$WF(a,b) = \langle F, \psi^{a,b}\rangle = \int_{-\infty}^{+\infty} F(t)a^{-1/2}\bar{\psi}\left(\frac{t-b}{a}\right)\mathrm{d}t, \tag{4}$$

where $\bar{\psi}$ denotes the complex conjugate of ψ.

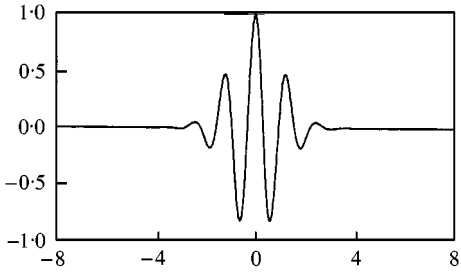

Figure 9. Morlet wavelet.

One can prove [10] that the wavelet transform is invertible and $F(t)$ is recovered with

$$F(t) = \frac{1}{C_\psi} \int_{-\infty}^{+\infty} \int_{0}^{+\infty} (WF)(a, b)\psi^{a,b}(t) \frac{\mathrm{d}a\,\mathrm{d}b}{a^2}. \tag{5}$$

The tailpipe microphone signals acquired during run-up are processed by using the CWT. The result is presented in Figure 10 where the lower plot corresponds to a signal captured in safe conditions such that there is no rasping noise generation while the upper plot is derived from a signal captured during metallic noise generation. The mother wavelet used here is the Morlet's one [11] whose expression is given in equation (6) and whose shape is presented in Figure 9:

$$\psi(t) = \mathrm{e}^{-t^2/2} \cos(5t). \tag{6}$$

This wavelet has an analytic presentation resembling the Gabor function that exhibits the Gaussian wavelet which is found to be the most fitted to detect singularities in signals [12]. It is commonly used to detect detonations in maladjusted engines [13]. The modulus of wavelet coefficients $C_{a,b}$ is computed at each scale a over the time axis defined by the parameter b. The procedure is started from small scales ($a = 2^0$) and continues toward higher scales ($a = 2^9$) in a geometric progression with factor $2^{0.25}$. Translated in terms of the frequency domain, the analysis starts from high frequencies (16·384 kHz) and proceeds towards low frequencies (32 Hz). The coefficient values are exhibited by a grey scaled colour where the black and white points indicate that the wavelet transform has respectively zero and positive values.

The upper plot of Figure 10 exhibits a large amount of non-zero wavelet coefficient values characterizing the rasping occurrence. They are presented by white and/or grey points reaching small scales until $a = 2$ corresponding to frequencies reaching 8 kHz. The rasping noise in that case is in full exhibition for an engine rotational speed higher than 3400 r.p.m. One can also notice grey points for lower engine speed which appear for larger but decreasing values of scales between 2^5 and 2^3. Otherwise, the result obtained in the no-rasping case presented in the lower graph of Figure 10 shows that the wavelet expansion coefficients have completely vanished for scale values lower than 2^5. The oblique lines shown in the lower graph of Figure 4 are translated here into a white area structured in logarithmic lines and observed at high scales. The order contents of the signal is then observed with wavelet analysis. The examination of these logarithmic lines show that harmonic H2 is dominating the signal at low engine

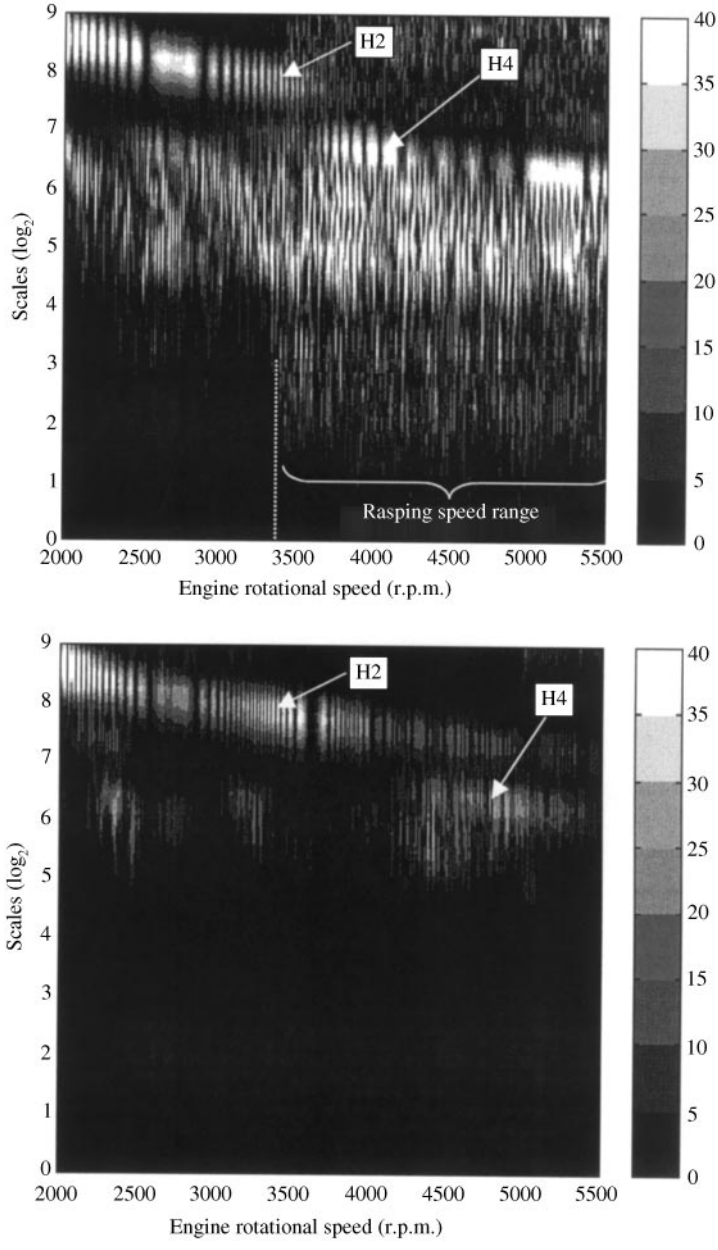

Figure 10. CWT of a signal captured in rasping case. Plot of the wavelet coefficients modulus C_{ab} using a linear scale. Upper, rasping case; lower, no rasping case.

speed and is replaced by harmonic H4 which emerges for high engine speed, beyond 4500 r.p.m.

The CWT results are in good agreement with those of STFT and order analysis. According to all these analyses, the rasping noise is well detected. However, in the fast run-up case, CWT which is well adapted to analyze non-stationary signals gives a more confident time localization of frequencies contained in a signal.

4.2. DISCRETE WAVELET TRANSFORM (DWT)

The main disadvantage of using CWT is the large computation time needed to calculate the wavelet coefficients. The discrete wavelet transform (DWT) reduces the time computation and should provide sufficient information to analyze fully both the low and the high frequencies of a signal.

4.2.1. *Multiresolution analysis*

In section 4.1 the resolution is defined as the inverse of the continuous scale parameter a. The multiresolution approximations compute the approximation of signals at various discrete resolutions. It consists of the computation of the orthogonal projections of the signal on a set of subspaces $\{V_j / V_j \subset L^2(\Re)\}_{j \in Z}$. The closed subspaces V_j satisfy

$$\{0\} = V_{+\infty} \subset \cdots \subset V_2 \subset V_1 \subset V_0 \subset V_{-1} \subset V_{-2} \subset \cdots \subset V_{-\infty} = L^2(\Re) \tag{7}$$

such that V_{j+1} is obtained from V_j by a factor 2 rescaling. Dyadic sequence is then generated. It satisfies a geometric progression with ratio 2. Thus

$$\forall j \in Z, \quad F(t) \in V_j \Leftrightarrow F\left(\frac{t}{2}\right) \in V_{j+1}. \tag{8}$$

V_j is also invariant under any translation. So

$$\forall (j, n) \in Z^2, F(t) \in V_j \Leftrightarrow F(t - n) \in V_j. \tag{9}$$

This leads to a series of approximations with resolutions 2^{-j} [14].

4.2.1.1. *Scaling functions.* Property (7) proves that an approximation at a resolution 2^{-j} contains all the necessary information to compute an approximation at coarser resolution 2^{-j+1}. Properties (8) and (9) imply that there exists $\varphi \in V_0$ such that the family $\{\varphi(t - n); n \in Z\}$ makes an orthonormal basis of V_0 so that the family of functions $\{\varphi_{j,n}; n \in Z\}$ defined as

$$\varphi_{j,n}(t) = 2^{-j/2} \varphi(2^{-j} t - n) \tag{10}$$

makes an orthonormal basis of V_j. The functions $\varphi_{j,n}$ are called scaling functions.

According to property (7) and the fact that $\{V_j / j \in Z\}$ is a dyadic sequence, $\varphi(t/2) \in V_1 \subset V_0$ for every scaling function $\varphi(t) \in V_0$. Thus, using the fact that the family $\{\varphi_{0,n}(t) = \varphi(2^0 t - n) / n \in Z\}$ makes an orthonormal basis of V_0, one obtains

$$\varphi\left(\frac{t}{2}\right) = \sum_{n \in Z} h[n] \varphi(t - n), \tag{11}$$

with

$$h[n] = \left\langle \varphi\left(\frac{t}{2}\right), \varphi(t - n) \right\rangle. \tag{12}$$

The sequence $h[n]$ is interpreted as a discrete filter and hence any scaling function is specified by a discrete filter called a conjugate mirror filter.

When dealing with compact support wavelets, there exists an integer n_0 such that for every n in Z with $|n| \geqslant n_0$ the support of $\varphi(t/2)$ and the support of $\varphi(t-n)$ are out-of joint, and hence the scalar product in equation (12) becomes null, so, the sum in equation (11) is a finite summation

$$\varphi\left(\frac{t}{2}\right) = \sum_{n=0}^{n=n_0-1} h[n]\varphi(t-n). \tag{13}$$

The Fourier transform of equation (11) gives

$$\hat{\varphi}(2\omega) = \hat{b}(\omega)\hat{\varphi}(\omega), \tag{14}$$

where $\hat{\varphi}(\omega)$ denotes the Fourier transform of $\varphi(t)$ and

$$\hat{h}(\omega) = \sum_{n\in Z} h[n]\mathrm{e}^{-\mathrm{i}n\omega}. \tag{15}$$

As equation (15) shows, $\hat{h}(\omega)$ is a 2π periodic function in $L^2([0-2\pi])$. By doing so on equation (14) and using the fact that $\hat{\varphi}(0) = 1$, one obtains

$$\hat{\varphi}(2\omega) = \hat{h}(\omega)\varphi(\omega) = \hat{h}(\omega)\hat{h}\left(\frac{\omega}{2}\right)\hat{\varphi}\left(\frac{\omega}{2}\right) = \cdots = \prod_{n=0}^{\infty} \hat{h}\left(\frac{\omega}{2^n}\right)\hat{\varphi}(0) = \sum_{n=0}^{\infty} \hat{h}\left(\frac{\omega}{2^n}\right). \tag{16}$$

Now proceeding with the inverse Fourier transform in equation (16) should give one the scaling function $\varphi(t)$.

4.2.1.2. *Wavelet mother function.* For every $j \in Z$ as $V_j \subset V_{j-1}$, let W_j be the orthogonal complement of V_j in V_{j-1}. One then has

$$V_{j-1} = V_j \oplus W_j, \tag{17}$$

where $\oplus$ denotes the gathering operator. According to Mallat and Meyer [15, 16] one can then construct for any scale 2^j an orthonormal basis $\psi_{j,n}$ of W_j such that

$$\psi_{j,n}(t) = 2^{-j/2}\psi(2^{-j}t - n), \tag{18}$$

where $\psi(t)$ is the mother wavelet whose Fourier transform satisfies

$$\hat{\psi}(\omega) = \frac{1}{\sqrt{2}}\hat{g}\left(\frac{\omega}{2}\right)\hat{\varphi}\left(\frac{\omega}{2}\right), \tag{19}$$

with

$$\hat{g}(\omega) = \mathrm{e}^{-\mathrm{i}\omega}\overline{\hat{h}}(\omega + \pi). \tag{20}$$

Calculating the inverse Fourier transform of equation (20) yields

$$g[n] = (-1)^{1-n}h[1-n]. \tag{21}$$

$g[n]$ is called a mirror filter. Equation (19) is the scaling equation. The wavelet $\psi(t)$ is hence determined by applying the inverse Fourier transform to $\hat{\psi}(\omega)$.

By doing so on equation (17), one can prove that $L^2(\Re)$ can be decomposed with orthogonal subspaces W_j. One hence has

$$L^2(\Re) = \bigoplus_{j \in Z} W_j. \tag{22}$$

So, the family $\psi_{j,n}$ make an orthonormal basis of $L^2(\Re)$ and ψ is called an orthogonal wavelet.

4.2.1.3. *Signal decomposition using filter banks.* Since $\{\varphi_{j,n}/n \in Z\}$ and $\{\psi_{j,n}/n \in Z\}$ are orthonormal bases of V_j and W_j the projection for each f in $L^2(\Re)$ in these spaces V_j and W_j yields

$$a_j[n] = \langle f, \varphi_{j,n} \rangle, \qquad d_j[n] = \langle f, \psi_{j,n} \rangle, \tag{23, 24}$$

where $a_j[n]$ is a discrete approximation of f and $d_j[n]$ is the remaining detail at scale 2^j. One can prove that $a_j[n]$, respectively $d_j[n]$, result from filtering $a_{j-1}[n]$ by $h[n]$ and $g[n]$ followed by factor 2 sub-sampling:

$$a_{j+1}[k] = a_j * \bar{h}[2k] = \sum_{n=0}^{n_0} a_j[n] h[n - 2k], \tag{25}$$

$$a_{j+1}[k] = a_j * \bar{g}[2k] = \sum_{n=0}^{n_0} a_j[n] g[n - 2k]. \tag{26}$$

Here the star symbol denotes the covolution operator. Note that $h[n]$ and $g[n]$, respectively, constitute a low- and high-pass filter and that, for each scale 2^j, the sub-sampling of the approximation $a_{j-1}[n]$ divides the filters' cut-off frequency by 2. Indeed, at every level, the sub-sampling results in half the number of samples, and hence the half-time resolution. It also results in half the frequency band spanned, and hence doubles the frequency resolution.

4.2.2. *Wavelet packet decomposition*

The wavelet packet decomposition is a fast discrete wavelet transform based on the same principle as the multiresolution analysis (see Figure 11). However, both the approximation

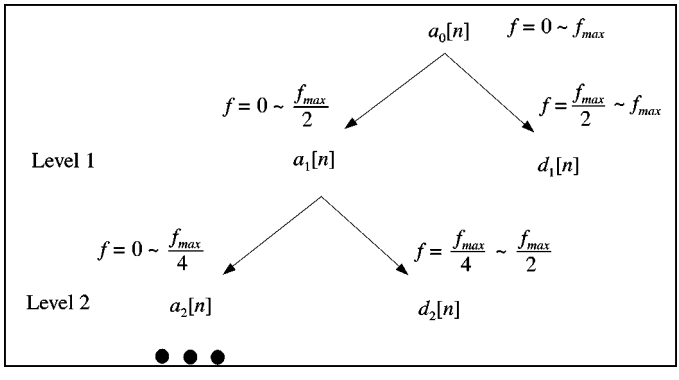

Figure 11. Algorithm of fast wavelet decomposition.

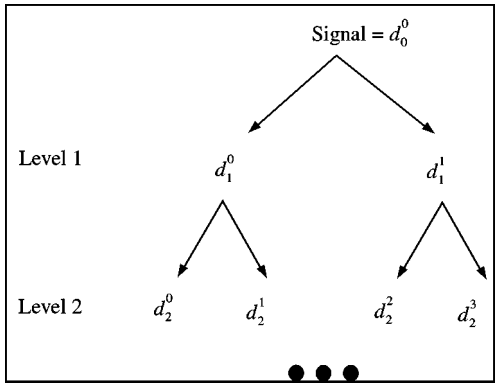

Figure 12. Wavelet packet tree.

spaces V_j and the detail spaces W_j are recursively subdivided into orthogonal subspaces W_j^p to derive new bases. The family wavelet packet $\psi_{j,n}^p$ such that

$$\{\psi_{j,n}^p = \psi_j^p(2^{-j}t - n)\}_{n \in Z}$$

constitutes an orthonormal basis of W_j^p. The decomposition is performed successively and then a binary tree as shown in Figure 12 is developed. Each node of the binary tree is labelled by (j, p) where j refers to the decomposition level and p refers to the rank of the node at each level. An increasing level j translates the refinement of the subdivision of the original signal ranging from slow to fast component, each one being ranked by the label p. It is shown that the wavelet basis corresponding to level $j + 1$ is derived from the level below by the following equation [14]:

$$\psi_{j+1}^{2p}(k) = \sum_{n=0}^{n_0} \psi_j^{2p}(2^{-j}k - n)h[n], \tag{27}$$

$$\psi_{j+1}^{2p+1}(k) = \sum_{n=0}^{n_0} \psi_j^{2p}(2^{-j}k - n)g[n]. \tag{28}$$

So for each function f in $L^2(\Re)$, the wavelet packet coefficients of a signal at a node (j, p) are obtained by the scalar product

$$d_j^p[n] = \langle f, \psi_{j,n}^p \rangle. \tag{29}$$

In decomposing an original signal the coefficients of wavelet packet children d_{j+1}^{2p} and d_{j+1}^{2p+1} are obtained by sub-sampling the convolutions of d_j^p with h^* and g^*:

$$d_{j+1}^{2p}[k] = d_j^p * \bar{h}[2k] = \sum_{n=0}^{n_0} d_j^p[n]h[n - 2k], \tag{30}$$

$$d_{j+1}^{2p+1}[k] = d_j^p * \bar{g}[2k] = \sum_{n=0}^{n_0} d_j^p[n]g[n - 2k]. \tag{31}$$

The procedure is similar to the fast wavelet decomposition described in the previous section. The original signal is passed through a highpass filter $h[n]$ to isolate the high-frequency components and through a low-pass filter $g[n]$ to isolate the low-frequency components. Then the obtained signals are subsampled by 2. The two details d_1^0 and d_1^1 at level 1 are then determined. To pass to level 2, d_1^0 and d_1^1 are decomposed by using the same operation to obtain d_2^0, d_2^1, d_2^2, and d_2^3 at level 3.

4.2.3. *Results*

The wavelet used in this study was the Daubechies one [17, 18] because of its aptitude to detect sudden change in signal characteristics. In this case the integer n_0 characterizing the order of the mother wavelet, evokes its regularity. The more regular a wavelet is, the more it is suitable to isolate the low-frequency components. Conversely, the less regular a wavelet is, the more it is suitable to isolate the high-frequency components. As all previous processing showed that in the rasping case, the tailpipe noise is widely spread over a large-frequency band including both slow and fast components, n_0 was chosen so as to have a compromise between both high- and low-frequency analysis. Several tests were performed and led to fixing $n_0 = 9$, which consists of using the Daubechies wavelet at order 5 (db5). The corresponding scaling and mother wavelet functions are presented in Figure 13. The wavelet decomposition of the tailpipe noise is performed by using five levels: $S = a_5 + d_5 + d_4 + d_3 + d_2 + d_1$.

Given that the original signal was sampled at 32·768 kHz allowing a frequency analysis until 16·384 kHz, the first level decomposition yields to a first detail d_1 approximately representing the frequency range (8·192–16·384 kHz), a second detail d_2 corresponding to (4·096–8·192 kHz) and so on until the fifth level whose detail d_5 corresponds to (512–1024 Hz). So the approximation a_5 at level 5 is filtered to frequencies lower than 512 Hz.

Figure 14 presents the result obtained in a rasping case which has to be compared to the no-rasping one presented in Figure 15. It is clearly observed that, while all details over order 4 have quite vanished in the no-rasping case, they have an amplitude merely ranging from 20 to 40% of the original signal in the rasping case. Details d_3 to d_1 highlight clearly the engine speed from which the metallic tone appears. They provide a confident criterion for the detection of rasping noise occurrence. The various tests performed during this study showed that d_1 provides a criterion which can be used to confirm that the tailpipe noise contains a rasping component while detail d_3 should be used to confirm that the signal corresponds to a normal tone. Otherwise, detail d_1 shows that the rasping noise was fully developed from engine speed equal to 3400 r.p.m. while detail d_3 shows that a large set of high harmonics arises from engine speed approximately equal to 3300 r.p.m.

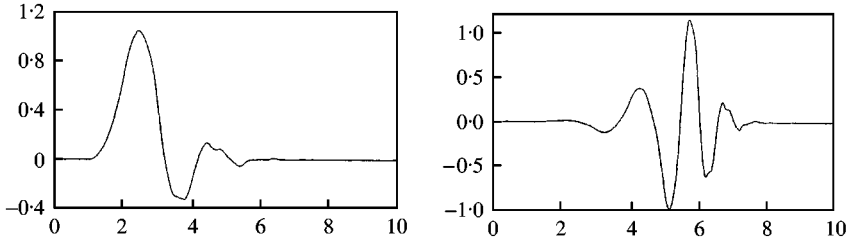

Figure 13. Daubechies wavelet. Left, scaling function; right, mother wavelet function.

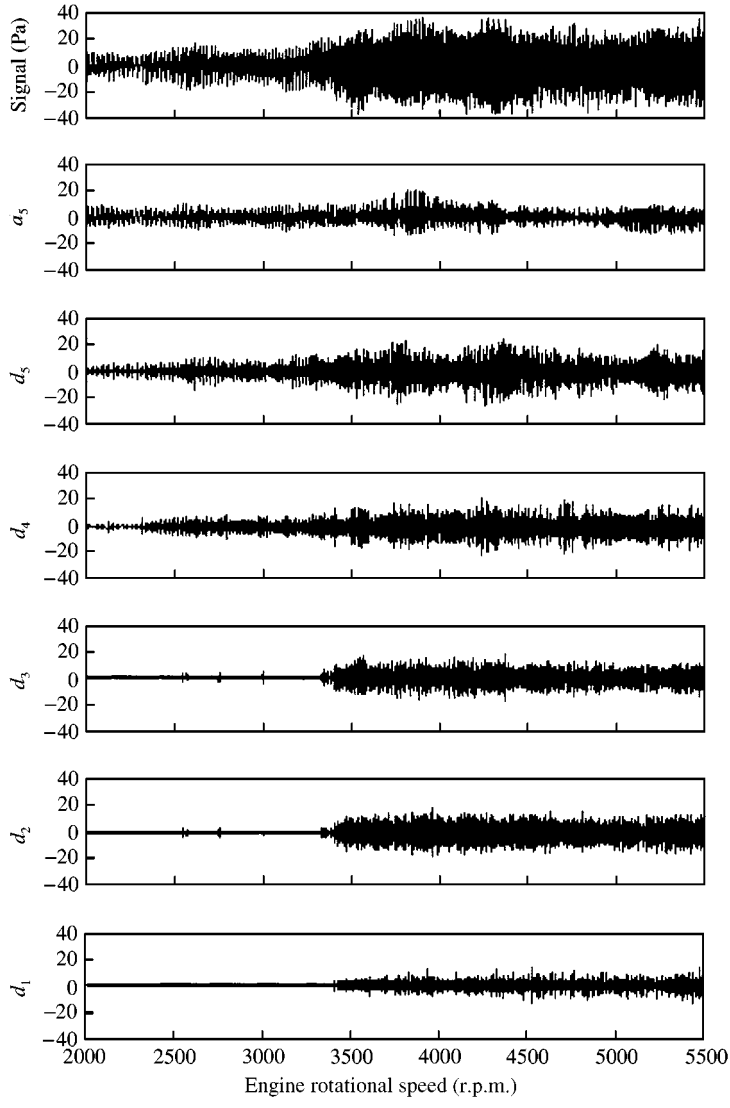

Figure 14. Multiresolution approximation of tailpipe noise in the rasping case.

When applying a wavelet packet decomposition using a packet filter bank at level 6, detail d_4 obtained by multiresolution analysis is split into four parts and the frequency resolution is refined to 256 Hz. In the rasping case, Figure 16 shows that outside the rasping speed range, d_4 decreases with respect to the frequency range; detail d_{43} and d_{44} levels are lower than 20% of the whole signal. Figure 17 presents the result obtained in the no-rasping case and also shows that only details d_{41} and d_{42} have a global level over 20% of the global signal, but in this case this level is reached at higher engine speed which means that, compared to the rasping case, it corresponds to lower harmonic order. Otherwise, in comparing both rasping and no-rasping cases, it is interesting to note that, as was observed with frequency analysis, high frequencies, e.g. high harmonic orders, are generated gradually from the beginning of the run-up, but this generation remains of low level ($\sim 10\%$ of the global level) and limited to 2 kHz until the rasping occurs.

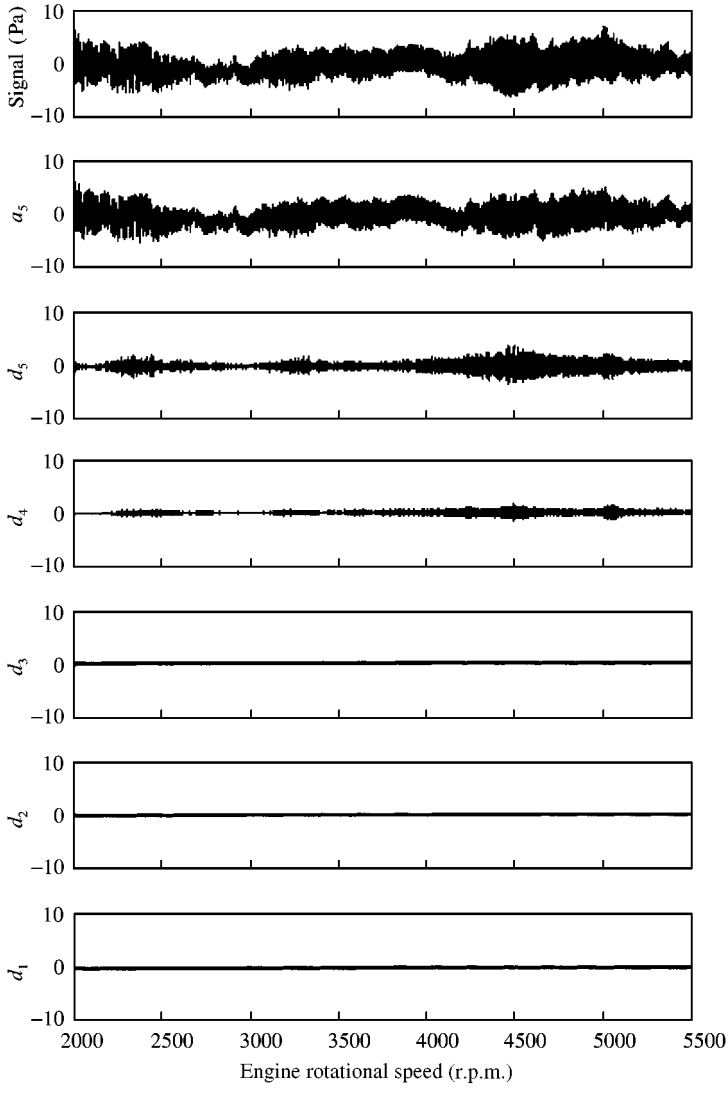

Figure 15. Multiresolution approximation of tailpipe noise in the no-rasping case.

5. RASPING RATE

It is proposed here to quantify the rasping rate produced by an exhaust pipe as the ratio of the power part corresponding to harmonics higher than a threshold one, to the total signal power. For this aim, the tailpipe noise was decomposed over a nine levels packet tree using Daubechies wavelet db5. This provides a frequency resolution equal to

$$\Delta f = \frac{16384}{2^9} = 32 \text{ Hz}.$$

At a given engine speed, the node of the 9th level that includes the threshold-harmonic is determined. So the power of the signal is split in two parts and the one corresponding to

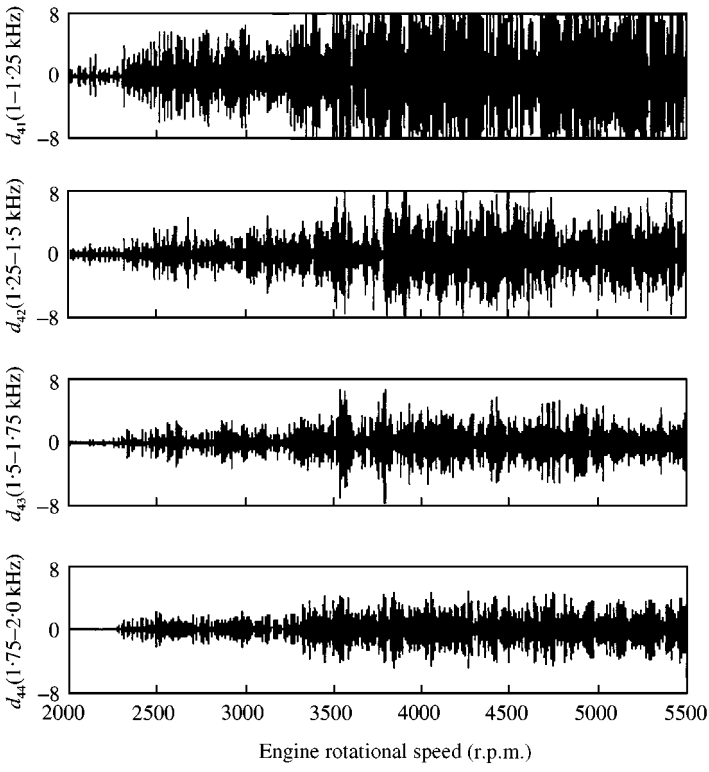

Figure 16. Rasping case—wavelet packet decomposition. Level 6 splits details d4 into four parts each one corresponding to a frequency range of 256 Hz.

higher order nodes is computed as a quadratic sum of wavelet transform coefficients

$$RR(\Omega) = \frac{\sum_{n > n_c(\omega)} (d_9^n)^2}{\sum_{n=1,2^9} (d_9^n)^2}, \tag{32}$$

where RR is the rasping rate, Ω is the engine rotational speed, d_9^n is the coefficient of the nth detail at level 9 after being ordered by increasing frequency range and n_c is the order of the detail whose frequency range includes the threshold harmonic.

Regarding the results of wavelet packet decomposition, threshold harmonic of orders 16, 24 and 30 have been selected to be tested. The results are presented in Figure 18. In the no-rasping case the result shows a very low rate of high-order component while this rate rises in the rasping case. The criterion using H16 as a threshold-harmonic rises less abruptly; it reaches 20% at low engine speeds in the rasping case and 5 to 10% in the no-rasping case. So it is not efficient to characterize the high-frequency component produced at the tailpipe. Otherwise, the result obtained with H24 and H30 as a harmonic threshold indicates almost the same rasping rate in rasping conditions but only the H30 criterion almost vanishes when the tail pipe is perceived as a normal one. It is the more selective one and may be used in design requirements to specify that the exhaust system should not produce a metallic tone. The efficiency of this criterion has been checked over a large set of experiments. All of them were performed with the same engine; nevertheless, the order of the harmonic threshold which allows the rasping rate quantification should remain unchanged for any classical four-stroke-four-cylinder engine.

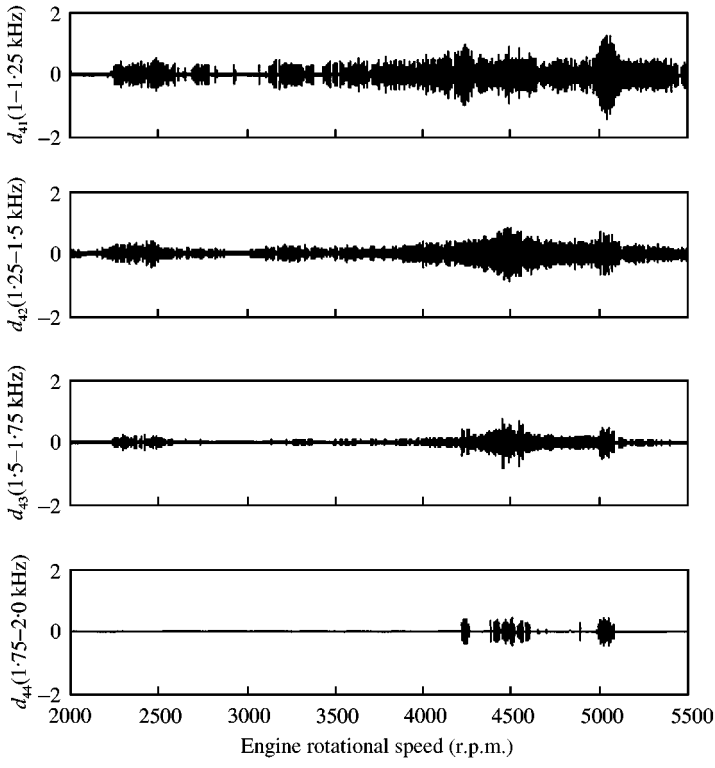

Figure 17. No-rasping case—wavelet packet decomposition. Level 6 splits details d4 into four parts each one corresponds to a frequency range of 256 Hz.

6. ACOUSTIC INTERPRETATION

In order to provide an acoustic interpretation of the efficiency of the criterion presented above, the internal pressure is examined in this section. As is shown in Figure 1, four piezoelectric pressure sensors have been used to measure the dynamic pressure at the outlet of the manifold and at three locations of the intermediate tube. The discrete wavelet decomposition has also been applied to the collected signals. Figure 19 shows the result obtained. Each graph presents simultaneously the original signal (black plot) superposed to detail d_3 (grey plot). Before applying the Daubechies wavelet decomposition, the original signal has been pre-processed in order to eliminate the static component and the stationary one. The stationary component is almost independent of the engine rotational speed and it particularly contains the flow noise. In all cases, the rate of energy retained after this pre-processing procedure is greater than 85% of the original signal energy. The upper graph of Figure 19 shows that detail d_3 of signal P_1 collected at the outlet of the manifold is very low which means that there is no rasping component generated by the engine. On the other hand, all signals collected inside the intermediate tube contain an important rasping component in the corresponding rotational speed range (see the tailpipe noise in the lower graph); this component rises when travelling along the tube. This remark is also valid for details d_2 and d_1 which characterize the rasping component in a more selective manner.

Figure 20 shows the time history of the collected internal pressures during two crank-shaft revolutions. Three samples are selected and presented in three columns of

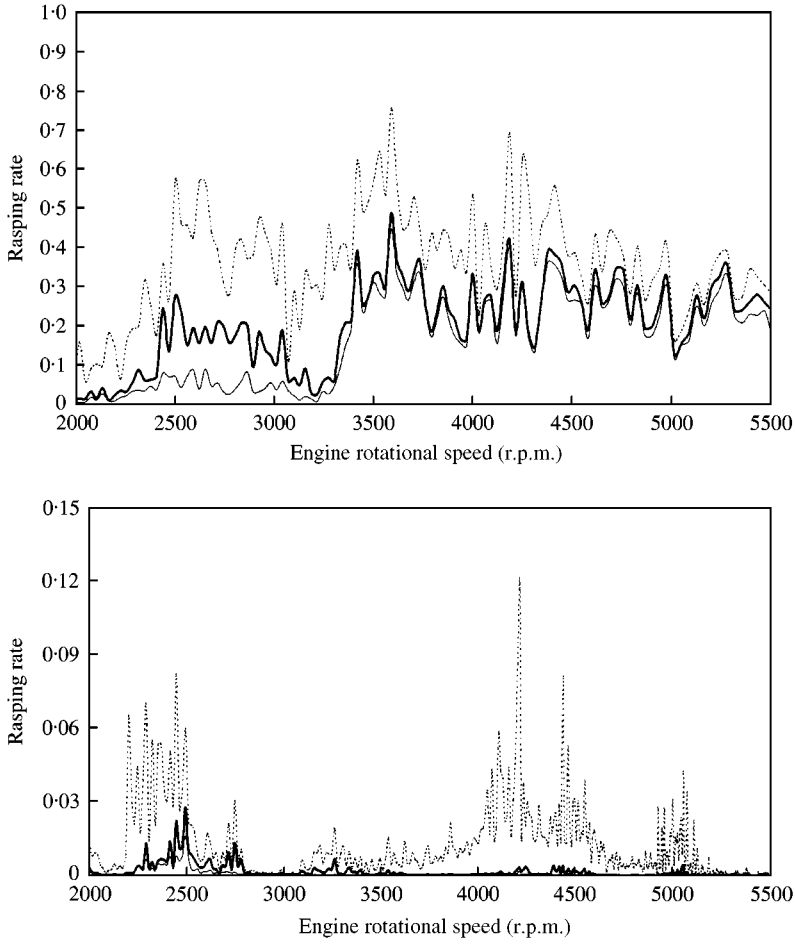

Figure 18. Rasping rate for various threshold harmonic order. Upper, rasping case; lower, no-rasping case; dotted line, H16; thick lines, H24; thin lines, H30.

graphs. The left column shows the signal collected at the beginning of the run-up. P_1 exhibits a classic four pulsation signal corresponding to the discharge (puff) and the repression of each cylinder [19, 9]. This is more or less the case of the pressure collected within the intermediate tube except the fact that the formation of standing waves tends to change the ratio between discharge and repression peak amplitudes. The second column shows the time signals collected at the beginning of the rasping noise generation (engine speed is equal to 3230 r.p.m.). The structure of pressure P_1 remains unchanged while a steepening of the waveform inside the pipe is clearly observed especially in the case of pressure P_3 collected at the middle of the tube. This is more clearly observed in Figure 21 which shows a comparison between the pressure waveform at rasping and no-rasping cases, at the same engine rotational speed. The waveform in the no-rasping case is symmetric while it is distorted in the rasping case: the signal grows faster, and then it decreases. This fact is less observable in the case of pressure P_2 and P_4 (Figure 20, second column, 3rd and 4th rows) because they are more sensitive to the reflected waves. In contrast, a high-frequency component that seems like a broadband noise is added to the pulsated noise. The third column graphs of Figure 20 present the collected signals when the rasping noise is fully

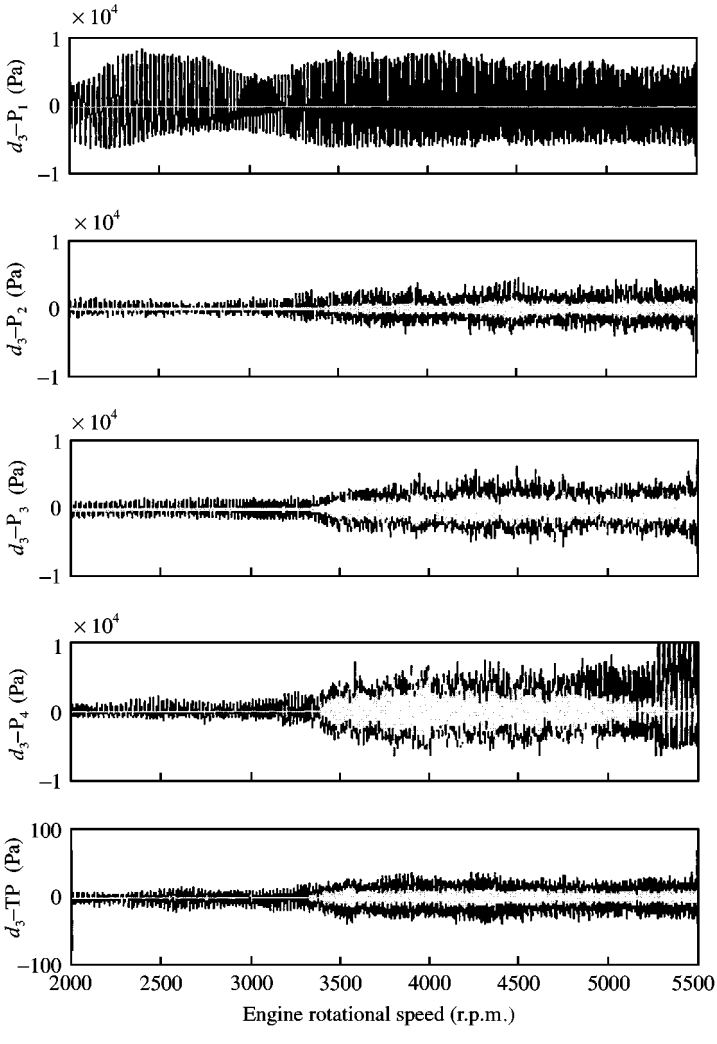

Figure 19. Internal pressure wavelet decomposition—Detail d3 (grey plot) compared to overall noise (black plot). Sensor 1 is located at the outlet of the manifold, sensor, 2–4 are respectively located at the entry, at the middle and at the bottom of the intermediate pipe. The lower graph corresponds to the tailpipe noise.

developed, at engine rotational speed equal to 4040 r.p.m. The waveform of pressure P_1 is no longer altered. Only a small broadband noise component which should be induced by the flow noise, is disturbing the pulsated signal. On the other hand, the pressures collected within the intermediate tube no longer have a pulsated waveform.

These observations indicate the development of a high-frequency component along the intermediate pipe. This behaviour represents the main feature of the rasping noise generation and should provide a physical interpretation of this phenomenon. In fact, both order and frequency analysis presented in section 3 have shown that, in the rasping case, a large set of resonance frequencies are excited and that the resulting component is dominating the high-frequency part of the signal. An interpretation of the rasping noise formation should probably consist of a non-linear resonance phenomena. During a run-up, the exhaust system resonance modes are successively excited. Thus, the acoustic pressure

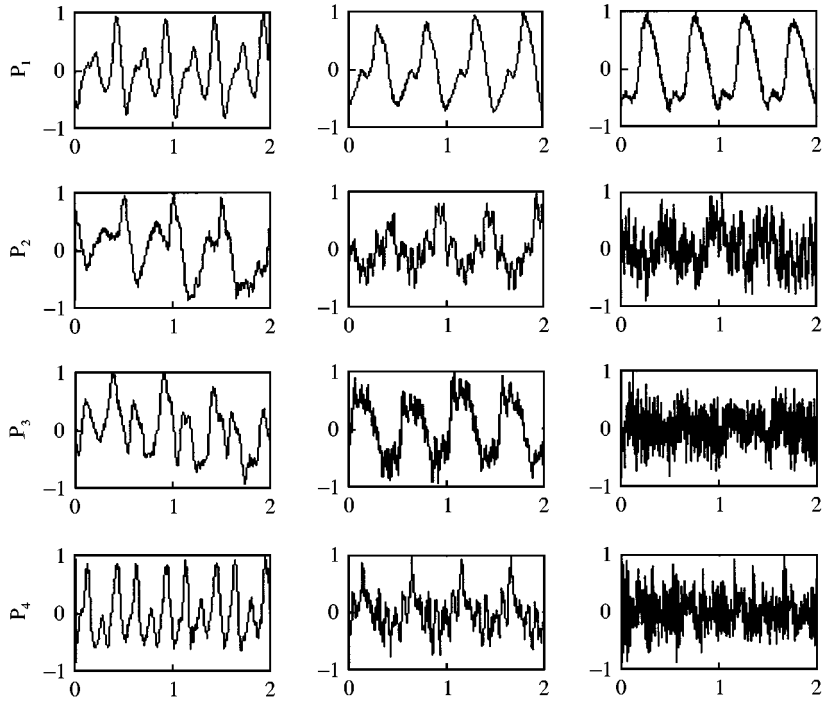

Figure 20. Internal pressure collected during two crank-shaft revolutions, centred and normalized to unity. From left to right, the engine rotational speed is respectively equal to 1700 r.p.m. (beginning of the acceleration), 3230 r.p.m. (beginning of the rasping speed bandwidth) and 4040 r.p.m. (rasping noise is fully developed).

may reach a high level so that the acoustic waves are propagating in a non-linear way [9, 1]. In cases of slow run-up, a resonance of the exhaust line is excited and attenuated by the dissipative effects before reaching the engine rotational speed which excites the following resonance. So, there is no significant coupling between resonance modes and the nonlinear effects remain negligible. On the other hand, in cases of abrupt engine acceleration, the time interval separating two engine speeds exciting a couple of resonance modes is so short that successive ones may occur almost simultaneously. This leads to a coupling between these resonance modes which makes them sustain each other. Therefore higher frequencies are abruptly generated.

This mechanism starts when a resonance frequency of the system meets a low harmonic of the engine rotational speed. In the case studied, the first resonance frequency of the intermediate pipe may be approximately bounded as follows:

$$f_{1\,min} = \frac{c}{4l} \approx \frac{600}{8} = 75 \text{ Hz} < f_1 < f_{1\,max} \approx \frac{c}{2l} \approx \frac{600}{4} = 150 \text{ Hz}.$$

Here c is the sound speed in the moving hot air (temperature equal to 500°C, Mach number equal to 0·1) and l is the length of the intermediate tube. This resonance frequency meets the harmonic H2 at engine rotational speed bounded by

$$\frac{60 f_{1min}}{2} = 2250 \text{ r.p.m.} < V_1 < \frac{60 f_{1\,max}}{2} = 4500 \text{ r.p.m.}$$

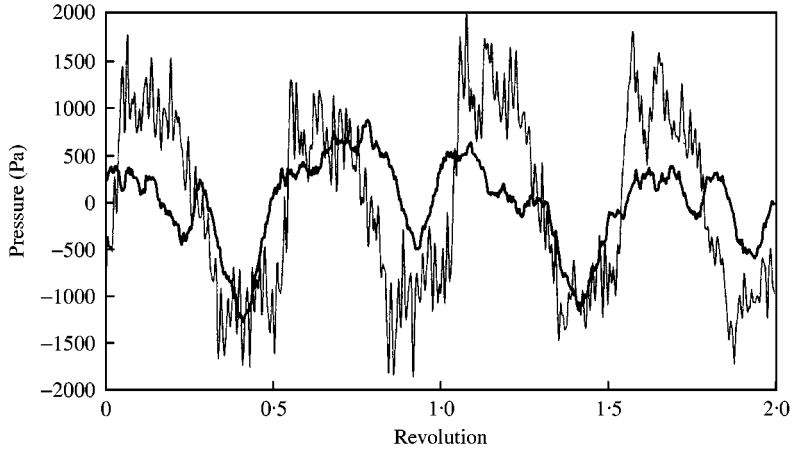

Figure 21. Internal pressure at the middle of the intermediate tube during two crank-shaft revolutions captured at an engine rotational speed of 3230 r.p.m. Thin lines, rasping case; thick lines, no-rasping case.

As was noticed, the rasping noise starts at an engine rotational speed around 3200 r.p.m. A large set of high frequencies are then developed in quasi-instantaneous manner and the rasping noise generation mechanical leads to an acoustic instability.

7. CONCLUSION

An experimental analysis of an abnormal exhaust noise is presented in this paper. The focus is on a metallic sound known as "rasping noise" which may be generated by an exhaust system during a rapid run-up synonymous with severe transient conditions. Three kinds of signal processing are tested: The frequency analysis based on discrete Fourier transform techniques showed that the rasping noise is characterized by very high-frequency components whose amplitudes are comparable to that of the low harmonics of the engine rotation. Besides the classic spectral analysis, a wavelet expansion is evaluated. It is shown to be an efficient tool to detect the occurrence of the abnormal noise and to isolate the high-frequency component despite the transient character of the signal. Thus, the discrete wavelet analysis provide a confident and objective judgement of the radiated sound quality.

The first level detail of the tailpipe signal sampled at 32 kHz should be used to confirm the occurrence of rasping noise. The third level detail is proposed as a more severe criterion enabling the designer to confirm that the exhaust line does not produce rasping noise. Moreover, a nine levels wavelet packet decomposition is used to assess the rasping within the tailpipe noise as the rate of energy spread over harmonics higher than a critical one. This estimator gives results that are in good agreement with the more detailed ones obtained by time-frequency and time-scale analysis. It also accurately corresponds with the subjective assessment perceived by a human ear. It should be useful for design specification definition. Moreover, it provides a suitable tool to analyze the physical feature of rasping noise. In a more general frame, it could be extended to characterize other non-linear behaviours encountered in piping systems acoustics.

An attempt is also made to analyze the physical mechanism responsible for rasping noise occurrence. The hypothesis that seems to be more realistic is based on a nonlinear behaviour. In that sense, it is in good agreement with previous works described in the

introduction. However, rather than a shock wave assumption, the authors favour the hypothesis of a balance between dissipative effects and non-linear coupling between exhaust system resonance modes which makes them sustain each other. This seems to be the more realistic assumption upon taking into account the fact that rasping noise is almost vanishing in the case of slow run-up and that it is not perceived at stabilized engine speed. Obviously, this assumption being based only on experimental results, has to be checked by using an analytical model. Such a model has to reproduce accurately the dissipative effects and has to take correctly into account a non-stationary source radiating in a bounded media.

REFERENCES

1. W. CHESTER 1964 *Journal of Fluid Mechanics* **18**, 44–64. Resonant oscillations in closed tubes.
2. A. HIRSCHBERG, J. KERGOMARD and G. WEINREICH 1996 *Mechanics of Musical Instruments*. Berlin: Springer.
3. A. HIRSCHBERG, J. GILBERT, R. MSALLAM and A. WIJNANDS 1996 *Journal of the Acoustical Society of America* **99**, 1754–1758. Shock waves in trombones.
4. Y. NIREI, T. KONOMI and H. NOHIRA 1991 *Toyota Technical Review* **41**, 29–34. Study on abnormal exhaust noise caused by shock wave and its improvement.
5. M. OKADA, T. ABE and M. INABA 1987 *Society of Automotive Engineers* **871924**, 3.943–3.954. Study of the generation mechanism for abnormal exhaust noise.
6. M. OKADA, S. MORIKAWA and T. ABE 1987 *JSAE Review* **8**, 34–39. Analysis of the generation mechanism for abnormal exhaust noise.
7. K. TAKAYAMA, O. ONODERA, N. SEKINE, K. ITO and S. MATSUMURA 1988 *Society of Automotive Engineers* **880082**. Shock wave development and propagation in automobile exhaust systems.
8. T. JONAS, P. GARCIA and C. KUNTZ 1994 *Society of Automotive Engineers* **945132**. Shell noise from car exhaust systems.
9. J. M. COULON 1994 *Ph.D. Thesis*, *University of Paris* 6, *Paris*. Caractérisation de l'ensemble moteur collecteur comme source acoustique vis a vis de l'échappement automobile.
10. K. CHUI 1992 *An Introduction to wavelets*. San Diego: Academic Press.
11. A. GROSSMAN and J. MORLET 1984 SIAM *Journal of Mathematics* **15**, 723–733. Decomposition of Hardy functions into integrable wavelets of constant shape.
12. S. MALLAT and W. L. HWANG 1992 *IEEE Transactions on Information Theory* **38**, 617–643. Singularity detection and processing with wavelets
13. H. KIKUCHI, M. NAKASHIZUKA and H. WATANABE 1992 *IEICE Trans. Fundamentals* **E75.A**, 980–987. Fast wavelet transform and its application to detecting detonation.
14. S. MALLAT 1998 *A Wavelet Tour of Signal Processing*. New York: Academic Press.
15. S. MALLAT 1987 *Transactions of the American Mathematics Society* **315**, 69–87. Multiresolution approximations and wavelet orthonormal bases of $\mathbf{L}^2(\Re)$.
16. Y. MEYER 1992 *Wavelet and Operators*; *Advanced Mathematics*. Cambridge: Cambridge University Press.
17. I. DAUBECHIES 1992 *Ten Lectures on Wavelets*. Philadelphia, PA: SIAM.
18. I. DAUBECHIES 1993 *Proceedings of Symposia in Applied Mathematics*, *American Mathematical Society*, *San Antonio*. Different perspectives on wavelets.
19. S. BENSON 1982 *The Thermodynamics and Gas Dynamics of Internal Combustion Engines*. Oxford: Oxford Science Publication.
20. O. V. RUDENKO and S. I. SOLUYAN 1977 *Theoretical Study of Non-Linear Acoustics*, (*Studies in Soviet Science*). New York: Plenum Press

APPENDIX A: NOMENCLATURE

dB	Decibel scale referenced to 20 μPa
Hn	harmonic of order n
$\bar{x}$	conjugate of x
$\hat{x}$	Fourier transform of x

x^*y	convolution product of x with y
$\oplus$	gathering symbol
WF	wavelet transform coefficient of function $F(t)$
$\Re$	set of real numbers
Z	set of integer numbers
$L^2(\Re)$	Hilbert space
φ	wavelet scaling function
ψ	wavelet mother function
$h(n)$	discrete conjugate mirror filter
$g(n)$	discrete mirror filter
a_k	kth detail in discrete wavelet multiresolution decomposition
d_k	kth approximation in discrete wavelet multiresolution decomposition
d_j^p	jth detail (node) of the pth level in discrete wavelet packet decomposition